Epigenetic Memory of Mouse Intestinal Inflammation

by

Albert T. Magnell

M.Biochem.
University of Oxford, 2015

SUBMITTED TO THE DEPARTMENT OF BIOLOGY
IN PARTIAL FULFILLMENT OF THE REQUIREMENTS
FOR THE DEGREE OF

MASTER OF SCIENCE IN BIOLOGY
AT THE
MASSACHUSETTS INSTITUTE OF TECHNOLOGY

FEBRUARY 2021

Signature of Author:_____
Department of Biology
January 15, 2021

Certified by:_____
Aviv Regev
Professor of Biology
Thesis Supervisor

Accepted by:_____
Amy Keating
Professor of Biology and Biological Engineering
Co-Director, Biology Graduate Program

Epigenetic Memory of Mouse Intestinal Inflammation

by

Albert T. Magnell

Submitted to the Department of Biology in Partial Fulfillment of the Requirements for the Degree of Master of Science in Biology at the Massachusetts Institute of Technology

Abstract

The gut, encompassing one of the largest epithelial surfaces in the body, interacts with both biological and non-biological agents that can cause regular injury. Fortunately, the small intestinal epithelium has a remarkable capacity to repair itself after severe injury, due to the abundance of highly replicative stem cells housed in the intestinal crypt regions. Much remains to be understood about the activation processes of the repair mechanisms and to what extent the stem cells themselves can adapt to certain forms of damage, including molecular mechanisms related to gene regulation. Here, I show that in response to acute inflammation, chromatin in intestinal stem cells has increased accessibility around specific loci and that this state is maintained in some regions even after the epithelium has recovered from damage, suggesting the possibility of memory. Such epigenetic memory may confer some adaptive resiliency to subsequent damage.

Thesis supervisor: Aviv Regev
Title: Core Member (on leave), Broad Institute; Professor of Biology (on leave)

Acknowledgements

I am extremely grateful to Aviv Regev for her mentorship in and out of the lab. I would also like to thank my prelim and thesis committee members, Drs. Laurie Boyer, Gene-Wei Li, Bob Sauer, and Omer Yilmaz for their guidance and the graduate program co-director, Dr. Amy Keating, for her support.

The Regev Lab is such an extraordinary group of brilliant and caring minds, and being a member has been a great honor. Among our current members and alumni, I would like to especially thank Moshe Biton, Christoph Muus, Brian Cleary, Eeshit Vaishnav, Carl de Boer, Josh Gould, and Eugene Drokhlyansky for their mentorship, insights, and good banter.

I would like to thank my parents for all the love they have shown me throughout my life and for supporting the indefatigable curiosity that keeps me going. Lastly, I would like to thank Maggie Solice, for all of her unwavering encouragement.

Table of Contents

Introduction

The small intestinal epithelium is the fastest regenerating tissue in the human body (Cheng and Leblond, 1974). Its turnover rate of 3-5 days is made possible by numerous pools of highly active intestinal stem cells (ISCs), marked by the Leucine-rich repeat-containing G-protein coupled receptor 5 (Lgr5), which replicate daily within the crypt regions (Barker et al., 2007). Through asymmetric cell divisions, these multipotent Lgr5+ ISCs give rise to every other epithelial cell type in the small intestine (Barker et al., 2007; Clevers, 2013). Located above the crypt base are transit amplifying (TA) progenitor cells, which divide even faster than their precursor ISCs. As the TA cells continue to differentiate, they progress upward in a "conveyor belt" fashion from the crypt, forming the villus (Kaur and Potten, 1986; Barker et al., 2008). The tip of the villus contains fully differentiated, post-mitotic cells. Because these cells are highly exposed to the digestive environment of the intestinal lumen, they are prone to abrasion and apoptosis. In a normal mouse intestine, approximately 1,400 cells are lost from each villus tip every day (Williams et al., 2015). Thus, a rapid rate of cell renewal ensures that the intestinal epithelium and, more broadly, the digestive process remain functional.

A further remarkable feature of the small intestinal epithelium is its endurance to severe damage and infection. A single surviving $Lgr5^{+}$ ISC is capable of repopulating its crypt and subsequently reforming a villus. The gut can also withstand the specific ablation of $Lgr5^{+}$ ISCs, replenishing them by reprogramming quiescent $Lgr5^{-}$ reserve stem cells and even more differentiated enterocytes and secretory cells (Tian et al., 2011; Tetteh et al., 2016; Jadhav et al., 2017; Santos et al., 2018). These repair mechanisms are facilitated by highly permissive chromatin regions

common among the different cell types (Kim et al., 2014). That is, despite the diversity of cells composing the crypts and villi, these cells contain many conserved regions of open chromatin that can be quickly expressed to differentiate cells. Much remains to be understood about the mechanisms behind this conversion process, but what is clear is that the epithelium has a large set of specialized tactics in anticipation of the many ways in which damage can arise.

Inflammation is one of the main causes of intestinal damage. The gut can be infected by many different types of pathogens, employing immune responses specialized to bacteria, viruses, and parasites, in addition to more generalized innate responses. Inflammation in the gut absent infection can even become a chronic condition, indicative of inflammatory bowel disease (IBD), spanning Crohn's disease. Elaborating the mechanisms that repair the intestinal epithelium post-inflammation should aid in our understanding of how to treat IBD. In mouse models, inflammation is often induced by treatment with dextran sodium sulfate (DSS), which has been well established as a means to model colitis symptoms in mice (Chassaing et al., 2014). Some healing mechanisms that specifically trigger in response to damage from DSS-induced inflammation have been identified in recent years. For example, the Toll-Like Receptor 4 was implicated in intestinal repair (Shi et al., 2019). Additionally, the ligand Slit2 and its receptor Robo1 were found to aid in repair by activating the autophagy of damaged $Lgr5^+$ ISCs (Xie et al., 2020).

Topologically akin to the gut, the skin faces similar challenges of damage at a constant pace. A novel adaptive mechanism observed in the skin may be at play in the gut. Skin epithelial stem cells can respond to acute inflammation by remodeling chromatin accessibility at key stress response gene loci, such as the inflammasome activator AIM2, which get expressed during the primary

response to inflammation. These chromatin regions are kept open even after the skin epithelium has fully recovered, so that in the event of subsequent inflammation, the important response genes can be activated more quickly. Surviving skin epithelial stem cells carry epigenetic memory of inflammation as an adaptation to future potential stresses (Naik et al., 2017; Naik et al., 2018). Remarkably, the relevant loci are maintained in an open chromatin state long after the system has recovered. When the skin is later reinjured, these open loci allow the system to heal at more than double the usual rate.

I hypothesized that $Lgr5^{+}$ ISCs may respond to intestinal inflammation in an analogous way, by maintaining epigenetic memory through open chromatin in key loci and that such an adaptive mechanism would help account for the small intestinal epithelium's resiliency. To test this hypothesis, I induced inflammation in the mouse gut using DSS and profiled chromatin in relevant cells. I asked whether chromatin regions in gene loci that are expressed in response to DSS-induced damage maintained in open states after the intestinal epithelium has healed. Such analysis should help identify faulty repair mechanisms of IBDs and, more broadly, contribute to our understanding of the dynamics of epigenetic adaptations.

Chapter 1: Physiological characterization of DSS-colitis inflammation and recovery

DSS has a detergent-like effect in the gut, destabilizing the protective mucus layers and permeabilizing the epithelium to bacterial infection. Acute inflammation reaches its peak after around 7 days of treatment. Histological imaging of treated tissue reveals erosion of the villi and extensive damage to the crypts. The loss of enterocytes means that the mouse cannot properly absorb nutrients in the small intestine. Damage to the colon results in diarrhea and the presence of blood in the stool. Weight loss of at least 10-15% occurs by the end of the treatment, and excessive dosing can lead to death (Chassaing et al., 2014). If treatment is halted and the mouse is allowed to recover, then the remaining ISCs can regenerate the epithelium, and the mouse will regain weight (Choi et al., 2015).

Because the potency of DSS is affected by several variables, including the mouse strain, sex, housing conditions, and the quality of the DSS batch (Eichele and Kharbanda, 2017), I first calibrated the DSS treatment. Typically, 1-3% DSS is used, so I initially opted for the midpoint, administering 2% DSS over 7 days to a wildtype mouse. However, I observed only 5% weight loss, suggesting that the treatment was too mild. Indeed, histological imaging of hemataoxylin and eosin (H&E) stained small intestine and colon samples revealed that the treatment tissue looked indistinguishable from control tissue. To induce more substantial inflammation, I next increased the dose to 3% DSS over 7 days, and observed a 13% weight loss, and considerable damage by histological imaging, with near-complete abrogation of the villi throughout the small intestine.

Next, I used the selected DSS treatment protocol on WT Lgr5-EGFP-IRES-creERT2 mice, and tracked how male and female mice recover from the treatment symptoms, monitoring weight and histology during treatment (**Figure 1**) and recovery (**Figure 2**) in control (n=2) and treated (n=6) mice. Overall, male mice responded more strongly to DSS treatment than females (18% vs. 13% maximal reduction on average), consistent with previous studies (Chassaing et al., 2014; Eichele and Kharbanda, 2017). By comparison, control mice exhibited little to no weight loss during the same period (0.9%). Similarly H&E staining of tissue samples from the upper and lower regions of the small intestine and from the colon (**Figures 3–5**), revealed damage incurred during DSS: Small intestinal villi were lost, with only the crypts remaining, and colon crypts displayed excessive growth and some damage, though the extent of the damage was less than in the small intestine. Weight was gained back to pre-treatment levels by 10 days after DSS treatment is stopped, consistent with tissue healing by H&E staining, such that small intestinal villi have regrown, and all of the crypts more closely resembled healthy ones (**Figures 3–5**). This speed of recovery is consistent with the 3-5 day turnover rate of healthy epithelium. Interestingly, the rate of weight gain was slower than of weight loss. Although the guts of the recovery mice looked relatively normal, it is possible that the DSS treatment directly or indirectly caused other forms of damage to the digestive system that, compared to the intestinal epithelium, took longer to heal.

<u>Figure 1:</u> Weights of mice during 3% DSS treatment.

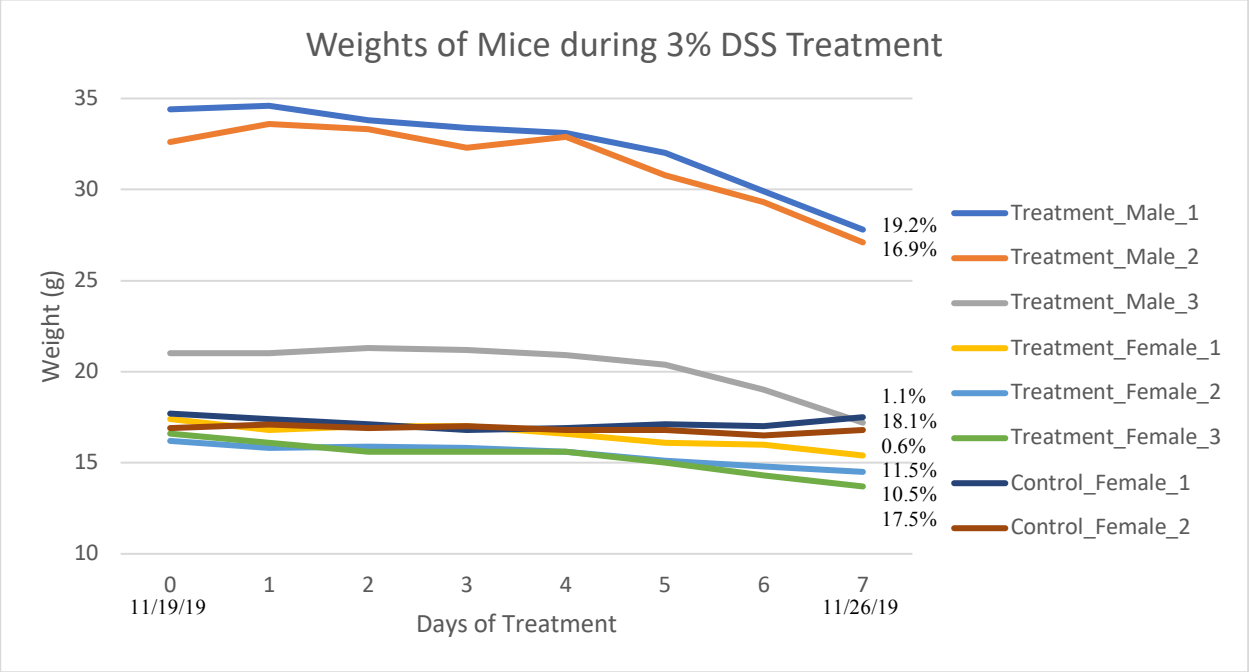

Weight (y axis, g) of individual DSS-treated mice and control mice during the time-course following the initiation of DSS treatment at day 0 (x axis). % weight losses depicted to the right of each curve are calculated by dividing the weight on day 7 by the weight on day 0, regardless of any temporary weight gain during the first two days of treatment. Weights were recorded every day from day 0 (November 19, 2019) through day 7 (November 26, 2019).

<u>Figure 2:</u> Weights of mice during recovery.

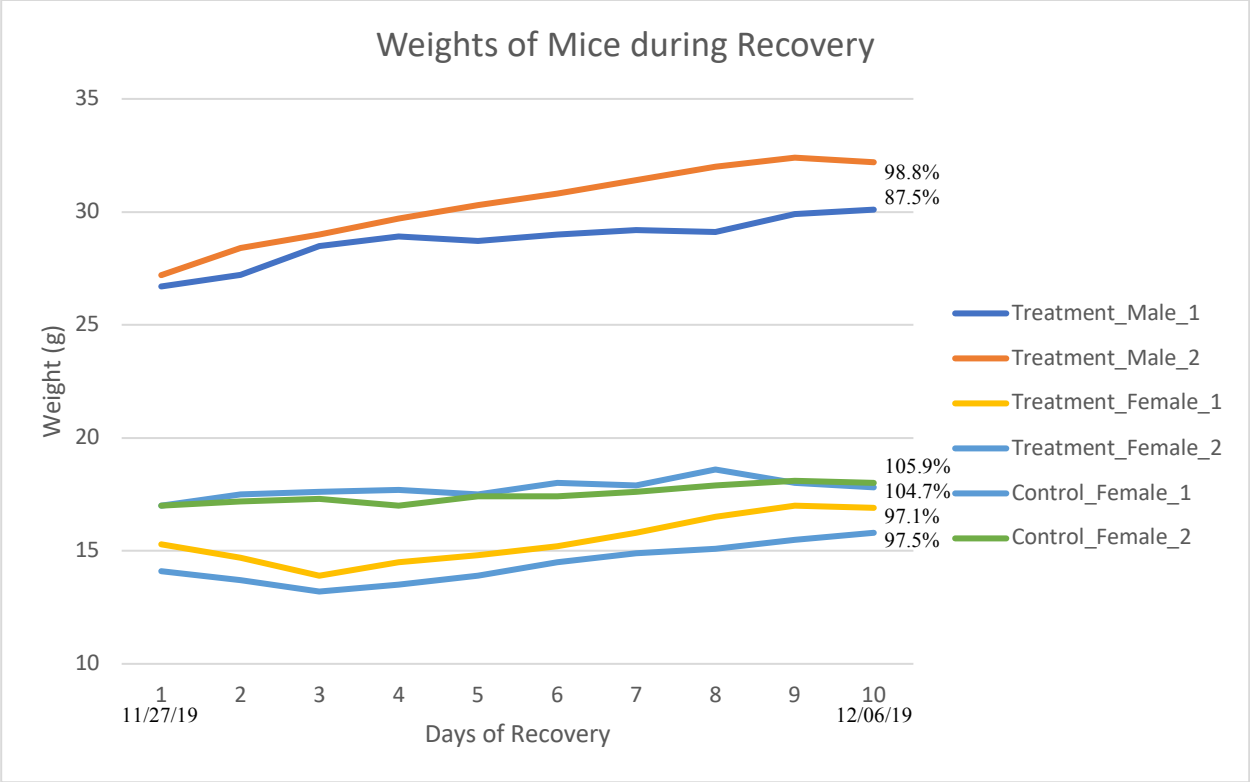

Weight (y axis, g) of individual DSS-treated mice and control mice during the recovery time-course following the stopping of DSS treatment (x axis). % weight losses depicted to the right of each curve indicate the percentage of weight at day 10 divided by the initial pre-treatment weight. Weights were recorded every day from day 1 (November 27, 2019) through day 10 (December 6, 2019). Treatment_Male_1 and Treatment_Female_1 mice, which were given 30 days of recovery, completely regained their initial weight by day 30.

<u>Figure 3:</u> Histology of healthy duodenum, ileum, and colon tissue.

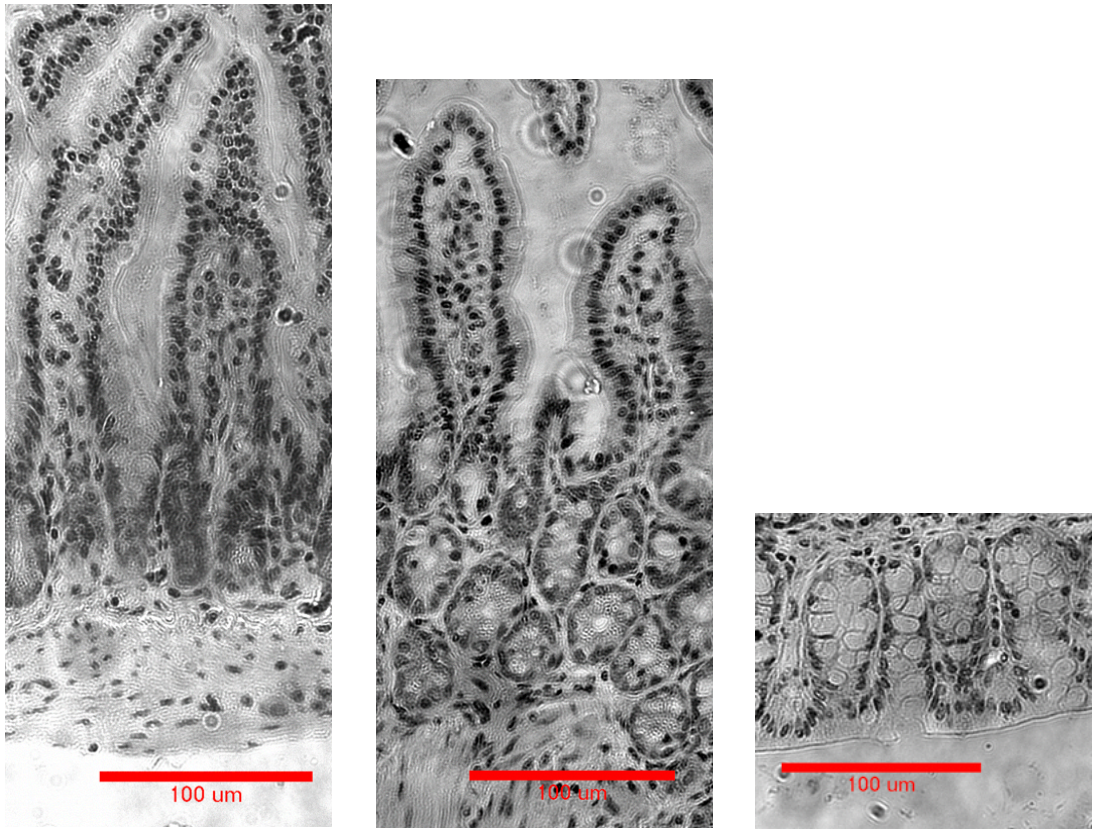

From left: H&E stains of healthy duodenum, ileum, and colon tissue sections from representative mice. Scale bar: 100μm

<u>Figure 4:</u> Histology of duodenum, ileum, and colon tissue at peak inflammation.

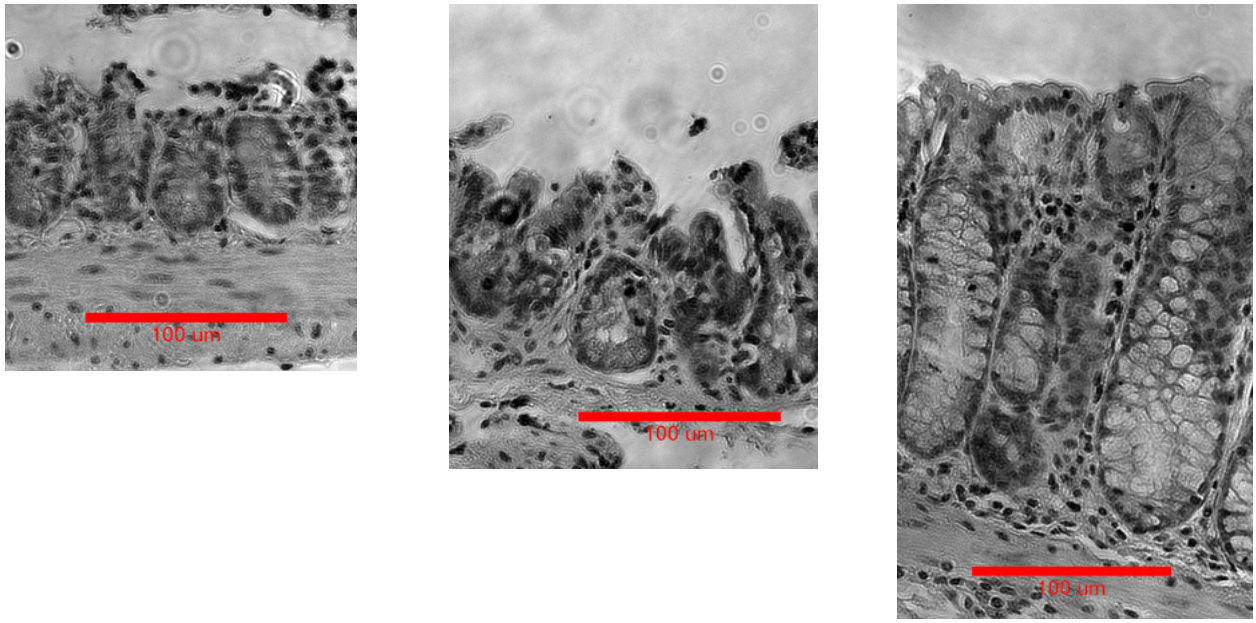

From left: H&E stains of duodenum, ileum, and colon tissue sections from representative mice at 7 days after initiation of DSS treatment. Scale bar: 100μm

<u>Figure 5:</u> Histology of duodenum, ileum, and colon tissue samples after 10 days of recovery.

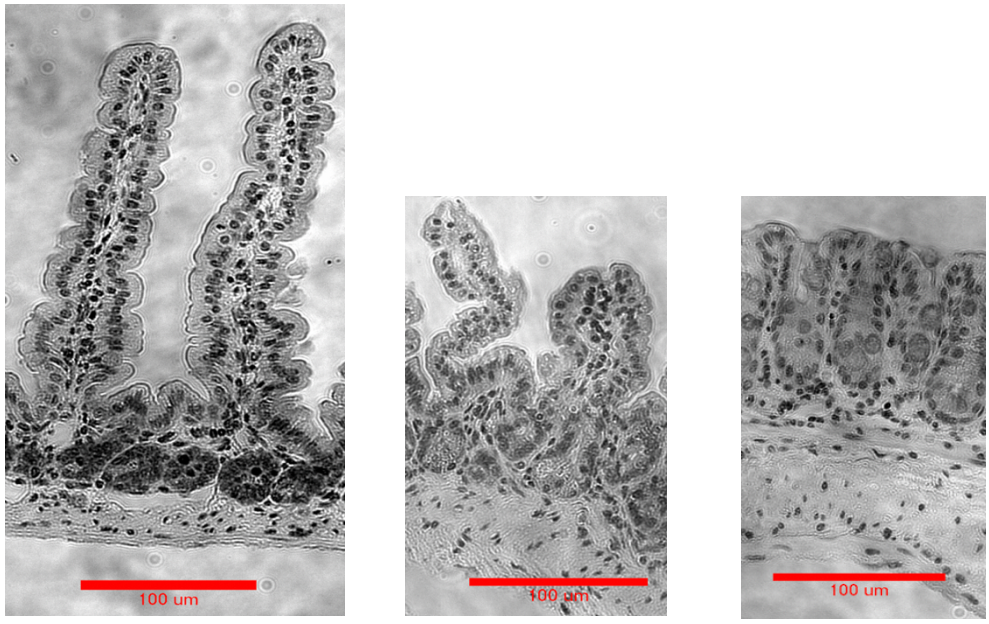

From left: H&E stains of duodenum, ileum, and colon tissue sections from representative mice at 10 days after stopping DSS treatment. Scale bar: 100μm

Chapter 2: Chromatin signatures of inflammation

At the peak of acute inflammation, surviving ISCs gain a temporary boost in their proliferative activity (Richmond et al., 2018). I hypothesized that such changes would be related to changes in chromatin organization. To test this hypothesis, I compared the chromatin profiles of crypt cells from mice experiencing severe inflammation against control mice that did not receive the DSS treatment. As shown in Chapter 1, after 7 days of imbibing DSS water, the treatment mice experienced significant weight loss and nearly lost all of their small intestinal villi. I harvested the remaining cells from the crypt regions alongside the crypt cells from healthy control mice. I then used bulk ATAC-seq (Buenrostro et al., 2015) to sequence specifically the DNA from open chromatin regions. The resulting sequence data of the treatment and control crypt cells were contrasted to identify sequence motifs that are more commonly found in the treatment cells. Such motifs can serve as binding sites for transcription factors that would therefore be potentially implicated in the crypt cells' response to inflammatory damage. By searching the sequence data for the locations of enriched motifs of interest, I was also able to identify genes whose expression they may regulate. This approach can be extended to establish putative mechanisms for cellular responses.

I hypothesized that the increased regeneration of ISCs would be reflected in increased chromatin accessibility in gene loci activated by relevant regulators. To test this hypothesis, I used HOMER to identify motifs differentially enriched in inflamed crypt cells relative to control crypt cells (**Figure 6**), and found enrichment of motifs for several transcription factors relevant to intestinal epithelial maintenance in loci preferentially open in cells from DSS-treated mice. The top two

most significantly enriched *de novo* motifs in DSS-treated samples were similar to the binding site for the SP2 transcription factor, which has been shown to reduce susceptibility to IBD by enhancing the expression of *Cd14*, which in turn enhances intestinal barrier function (Zschemisch et al., 2016; Buchheister et al., 2017), and to the HNF4a binding site, which regulates fatty acid oxidation and is critical for ISC renewal (Chen et al., 2020). The most significantly enriched known motif was a binding site for SP1, which regulates the basal activity of *Cd14* (Zschemisch et al., 2016). KLF family binding sites, in particular for KLF5, which supports gut epithelial barrier function by activating the expression of *Ascl2*, were also highly significantly enriched (Kim et al., 2017; Liu et al., 2017; Kim et al., 2020). Indeed, peaks around the *Ascl2* gene are enriched for the binding sites of KLF5 and Hnf4a (**Figure 7**), and those around *Cd14* contain enhancer sequences for Sp2 (**Figure 8**). Finally, Gene Ontology (GO) analysis of the top gene functions associated with the differentially accessible peak inflammation motifs corroborated the HOMER findings (**Figure 9**). Regulation of microvillus assembly and regulation of microvillus organization both showed >100-fold enrichment in the treatment cells. Thus, in response to DSS-induced inflammation, surviving crypt cells remodel their chromatin to increase the accessibility of several sequence motifs, potentially facilitating the binding of key transcription factors that promote ISC turnover and the subsequent regeneration of the microvilli. This supports my hypothesis that the repair process of the intestinal epithelium is accompanied by a set of epigenetic modifications. Whether these changes were in effect temporarily during inflammation or remained after recovery was the question I next sought to answer.

<u>Figure 6:</u> Motifs significantly associated with loci differentially accessible in peak inflammation vs. controls.

Rank	Motif	P-value	log P-pvalue	% of Targets	% of Background	STD(Bg STD)	Best Match/Details
1		1e-625	-1.441e+03	4.97%	2.94%	51.5bp (59.1bp)	Sp2(Zf)/HEK293-Sp2.eGFP-ChIP-Seq(Encode)/Homer(0.922) More Information | Similar Motifs Found
2		1e-417	-9.617e+02	46.44%	42.01%	51.5bp (57.0bp)	PB0134.1_Hnf4a_2/Jaspar(0.691) More Information | Similar Motifs Found
3		1e-343	-7.909e+02	1.31%	0.59%	45.3bp (57.1bp)	BORIS(Zf)/K562-CTCFL-ChIP-Seq(GSE32465)/Homer(0.908) More Information | Similar Motifs Found
4		1e-182	-4.205e+02	65.17%	62.33%	55.2bp (57.5bp)	RBMS1(RRM)/Homo_sapiens-RNCMPT00152-PBM/HughesRNA(0.705) More Information | Similar Motifs Found
5		1e-167	-3.861e+02	66.59%	63.89%	55.4bp (57.0bp)	Unknown2/Drosophila-Promoters/Homer(0.745) More Information | Similar Motifs Found
6		1e-164	-3.790e+02	10.16%	8.55%	53.7bp (57.0bp)	HNRNPA1L2(RRM)/Homo_sapiens-RNCMPT00023-PBM/HughesRNA(0.709) More Information | Similar Motifs Found
7		1e-162	-3.742e+02	2.50%	1.73%	52.9bp (55.9bp)	NFYA/MA0060.3/Jaspar(0.911) More Information | Similar Motifs Found
8		1e-153	-3.525e+02	51.26%	48.57%	54.7bp (56.1bp)	GATA19(C2C2gata)/colamp-GATA19-DAP-Seq(GSE60143)/Homer(0.879) More Information | Similar Motifs Found
9		1e-152	-3.505e+02	50.39%	47.71%	54.4bp (55.5bp)	GCN4/GCN4_SM/121-GCN4(Harbison)/Yeast(0.756) More Information | Similar Motifs Found
10		1e-128	-2.964e+02	1.35%	0.86%	53.2bp (59.3bp)	Elk1(ETS)/Hela-Elk1-ChIP-Seq(GSE31477)/Homer(0.984) More Information | Similar Motifs Found

Rank	Motif	Name	P-value	log P-pvalue	q-value (Benjamini)	# Target Sequences with Motif	% of Targets Sequences with Motif	# Background Sequences with Motif	% of Background Sequences with Motif
1		Sp1(Zf)/Promoter/Homer	1e-539	-1.243e+03	0.0000	7062.0	2.94%	3673.6	1.54%
2		KLF3(Zf)/MEF-Klf3-ChIP-Seq(GSE44748)/Homer	1e-491	-1.132e+03	0.0000	13878.0	5.78%	9066.6	3.79%
3		KLF5(Zf)/LoVo-KLF5-ChIP-Seq(GSE49402)/Homer	1e-491	-1.131e+03	0.0000	33072.0	13.77%	25509.7	10.66%
4		CTCF(Zf)/CD4+-CTCF-ChIP-Seq(Barski_et_al.)/Homer	1e-422	-9.729e+02	0.0000	4616.0	1.92%	2236.5	0.93%
5		Sp2(Zf)/HEK293-Sp2.eGFP-ChIP-Seq(Encode)/Homer	1e-401	-9.252e+02	0.0000	37006.0	15.40%	29729.9	12.42%
6		Sp5(Zf)/mES-Sp5.Flag-ChIP-Seq(GSE72989)/Homer	1e-367	-8.468e+02	0.0000	24074.0	10.02%	18411.1	7.69%
7		KLF6(Zf)/PDAC-KLF6-ChIP-Seq(GSE64557)/Homer	1e-366	-8.437e+02	0.0000	26026.0	10.83%	20146.1	8.42%
8		Klf4(Zf)/mES-Klf4-ChIP-Seq(GSE11431)/Homer	1e-355	-8.194e+02	0.0000	10942.0	4.55%	7272.2	3.04%
9		BORIS(Zf)/K562-CTCFL-ChIP-Seq(GSE32465)/Homer	1e-336	-7.757e+02	0.0000	5603.0	2.33%	3157.8	1.32%
10		Klf9(Zf)/GBM-Klf9-ChIP-Seq(GSE62211)/Homer	1e-267	-6.170e+02	0.0000	10205.0	4.25%	7084.7	2.96%

Top 10 *de novo* (top) and known (bottom) motifs significantly associated with loci that are differentially accessible in DSS-treated vs. control mice.

<u>Figure 7:</u> Motifs for the transcription factors KLF5 (GGGYGKGG) and Hnf4a (RNDVWGTNYD) in regions that are differentially accessible at the *Ascl2* locus in DSS treated vs. control mice.

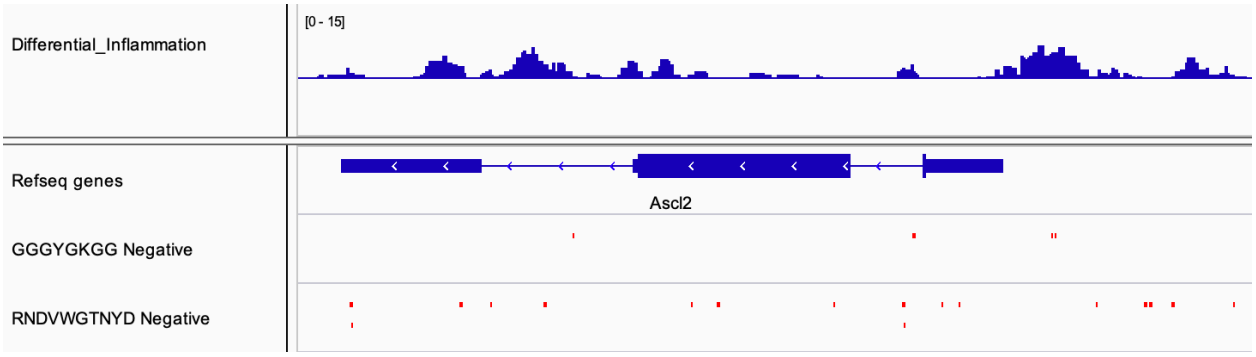

<u>Figure 8:</u> Motifs for the transcription factor Sp2 in regions that are differentially accessible at the *Cd14* locus in DSS treated vs. control mice.

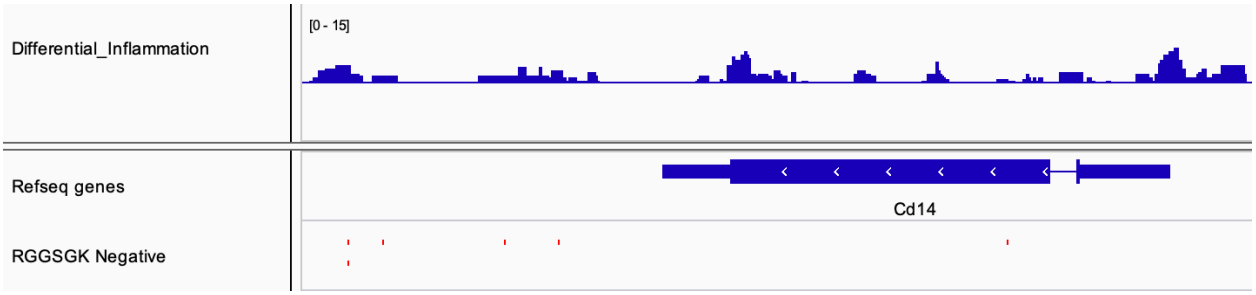

<u>Figure 9:</u> Functional categories enriched in genes with loci differentially accessible in DSS treated vs. control mice.

	Mus musculus (REF)	upload_1 (Hierarchy) NEW!					
GO biological process complete	#	#	expected	Fold Enrichment	+/-	raw P value	FDR
regulation of microvillus assembly	8	2	.01	> 100	+	7.30E-05	1.29E-02
embryonic process involved in female pregnancy	9	2	.01	> 100	+	8.92E-05	1.49E-02
regulation of microvillus organization	15	2	.02	> 100	+	2.20E-04	3.38E-02
positive regulation by host of viral transcription	16	2	.02	95.97	+	2.47E-04	3.73E-02
positive regulation of pri-miRNA transcription by RNA polymerase II	44	5	.06	87.25	+	4.75E-09	1.67E-06
regulation of gene expression by genetic imprinting	18	2	.02	85.31	+	3.06E-04	4.42E-02
regulation of pri-miRNA transcription by RNA polymerase II	56	6	.07	82.26	+	1.63E-10	7.19E-08
glandular epithelial cell development	19	2	.02	80.82	+	3.38E-04	4.79E-02
columnar/cuboidal epithelial cell development	63	3	.08	36.56	+	8.57E-05	1.45E-02
liver development	99	4	.13	31.02	+	9.34E-06	2.15E-03

Chapter 3: Chromatin signatures maintained through recovery

After 10 days of recovery, the intestinal epithelium appears fully healed, and at least one round of full cellular turnover has occurred, suggesting that many changes in chromatin accessibility will have reverted to their pre-treatment state. The retention of accessible loci after recovery could indicate an adaptive utility to protect against future damage. Using the same strategy as described in Chapter 2, I harvested the crypt cells from mice given 10 days of recovery after concluding the DSS treatment. I then performed bulk ATAC-seq (Buenrostro et al., 2015) on these cells, so that I could compare their open chromatin sequence data with the peak inflammation and control data sets.

To test for the possibility of epigenetic memory maintained after recovery, I used HOMER to identify differential chromatin accessibility in crypt cells from recovered vs. control mice (**Figure 10**). Known motifs significantly associated with higher chromatin accessibility in recovered vs. control mice include the binding sites for the transcription factors SP1, SP2, SP5, KLF3, KLF5, KLF6, and HNF4a, mirroring those in DSS treated mice, and suggesting that some features of chromatin accessibility are retained at least 10 days after stopping DSS treatment and when the tissue appears healed. Indeed, like the cells at peak inflammation, the cells after 10 days of recovery had peaks around the *Ascl2* gene enriched for the binding sites of KLF5 and Hnf4a (**Figure 11**) and peaks around the *Cd14* gene containing enhancer sequences for Sp2 (**Figure 12**). These results support my hypothesis that certain chromatin regions made accessible during inflammation to bolster epithelial repair remain accessible even after microvilli have been rebuilt and intestinal function is ostensibly normal. Similarly, d*e novo* motifs significantly enriched in

accessible loci in recovered vs. control mice include binding sites for SP1, ELF1 (known to regulate the expression of genes for intestinal growth and homeostasis), and CREM (**Figure 13**) (which enhances the expression of IL-21, a well-known IBD marker (Jedlicka and Gutierrez-Hartmann, 2008; Ohl et al., 2016)). Furthermore, GO analysis of the top gene functions associated with the differentially accessible regions in recovered vs. control mice showed enrichment in regulation of microvillus assembly and microvillus organization (**Figure 14**). Lastly, while there may be some changes in chromatin accessibility that arise specifically during the recovery period, there were much less significant differential enrichment between the motifs in cells from recovered vs. DSS treated mice, particularly among known motifs (**Figure 15**). Overall, these results suggest that key changes in the chromatin accessibility in crypt cells that arise during inflammation persist after the intestinal epithelium regenerates for at least 10 days. This supports my hypothesis that this chromatin remodeling may serve as a long-term adaptation to help the small intestine recover from future inflammatory damage more quickly.

<u>Figure 10:</u> Motifs significantly associated with loci differentially accessible in recovered vs. control mice.

Rank	Motif	P-value	log P-pvalue	% of Targets	% of Background	STD(Bg STD)	Best Match/Details
1		1e-56	-1.300e+02	0.07%	0.00%	50.6bp (28.0bp)	OPI1/MA0349.1/Jaspar(0.660) More Information | Similar Motifs Found
2		1e-41	-9.665e+01	0.06%	0.00%	52.6bp (0.0bp)	ELF1/MA0473.2/Jaspar(0.810) More Information | Similar Motifs Found
3		1e-41	-9.464e+01	0.52%	0.22%	53.8bp (58.8bp)	Sp1(Zf)/Promoter/Homer(0.969) More Information | Similar Motifs Found
4		1e-36	-8.450e+01	0.06%	0.00%	53.4bp (91.8bp)	NRF1(NRF)/MCF7-NRF1-ChIP-Seq(Unpublished)/Homer(0.852) More Information | Similar Motifs Found
5		1e-31	-7.219e+01	0.05%	0.00%	58.3bp (29.6bp)	MYB118(MYB)/colamp-MYB118-DAP-Seq(GSE60143)/Homer(0.714) More Information | Similar Motifs Found
6		1e-30	-6.978e+01	0.06%	0.00%	48.6bp (30.3bp)	FRS9(ND)/col-FRS9-DAP-Seq(GSE60143)/Homer(0.682) More Information | Similar Motifs Found
7		1e-29	-6.818e+01	0.07%	0.01%	52.6bp (46.1bp)	PUM(PUF)/Drosophila_melanogaster-RNCMPT00102-PBM/HughesRNA(0.716) More Information | Similar Motifs Found
8		1e-29	-6.691e+01	0.05%	0.00%	60.8bp (42.1bp)	CRF10(AP2EREBP)/col100-CRF10-DAP-Seq(GSE60143)/Homer(0.722) More Information | Similar Motifs Found
9		1e-27	-6.408e+01	0.05%	0.00%	58.7bp (53.1bp)	T1ISRE(IRF)/ThioMac-Ifnb-Expression/Homer(0.717) More Information | Similar Motifs Found
10		1e-27	-6.219e+01	0.04%	0.00%	50.9bp (0.0bp)	Crem/MA0609.1/Jaspar(0.890) More Information | Similar Motifs Found

Rank	Motif	Name	P-value	log P-pvalue	q-value (Benjamini)	# Target Sequences with Motif	% of Targets Sequences with Motif	# Background Sequences with Motif	% of Background Sequences with Motif
1		Sp1(Zf)/Promoter/Homer	1e-26	-6.155e+01	0.0000	823.0	1.31%	551.3	0.88%
2		Ronin(THAP)/ES-Thap11-ChIP-Seq(GSE51522)/Homer	1e-19	-4.589e+01	0.0000	117.0	0.19%	43.7	0.07%
3		KLF5(Zf)/LoVo-KLF5-ChIP-Seq(GSE49402)/Homer	1e-18	-4.355e+01	0.0000	5416.0	8.61%	4798.8	7.64%
4		Sp2(Zf)/HEK293-Sp2.eGFP-ChIP-Seq(Encode)/Homer	1e-16	-3.896e+01	0.0000	6115.0	9.72%	5496.7	8.75%
5		KLF6(Zf)/PDAC-KLF6-ChIP-Seq(GSE64557)/Homer	1e-15	-3.552e+01	0.0000	4285.0	6.81%	3788.5	6.03%
6		Sp5(Zf)/mES-Sp5.Flag-ChIP-Seq(GSE72989)/Homer	1e-14	-3.317e+01	0.0000	3814.0	6.06%	3361.1	5.35%
7		BORIS(Zf)/K562-CTCFL-ChIP-Seq(GSE32465)/Homer	1e-12	-2.819e+01	0.0000	707.0	1.12%	534.6	0.85%
8		SeqBias: polyA-repeat	1e-11	-2.606e+01	0.0000	62470.0	99.34%	62219.7	99.09%
9		KLF3(Zf)/MEF-Klf3-ChIP-Seq(GSE44748)/Homer	1e-11	-2.586e+01	0.0000	1930.0	3.07%	1648.5	2.63%
10	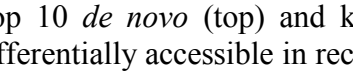	HNF4a(NR),DR1/HepG2-HNF4a-ChIP-Seq(GSE25021)/Homer	1e-10	-2.427e+01	0.0000	2685.0	4.27%	2362.8	3.76%

Top 10 *de novo* (top) and known (bottom) motifs significantly associated with loci that are differentially accessible in recovered vs. control mice.

Figure 11: **Motifs for the transcription factors KLF5 (GGGYGKGG) and Hnf4a (RNDVWGTNYD) in regions that are differentially accessible at the *Ascl2* locus in recovered vs. control mice.**

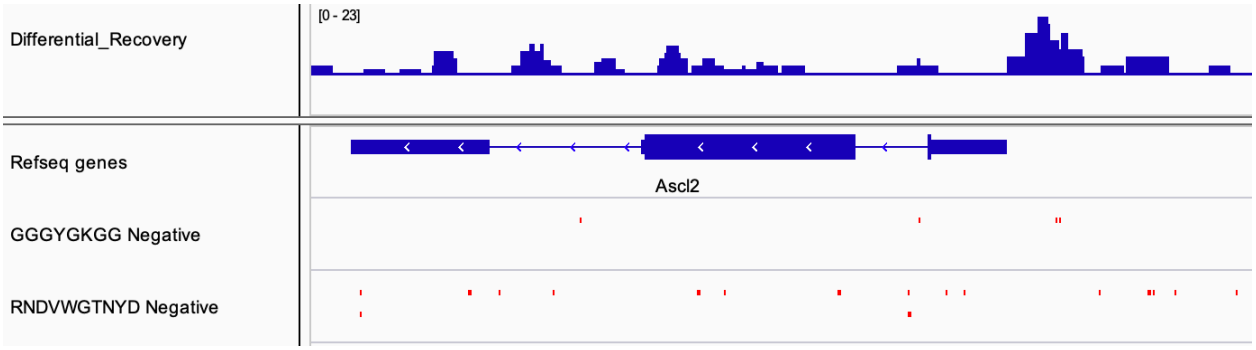

Figure 12: **Motifs for the transcription factor Sp2 in regions that are differentially accessible at the *Cd14* locus in recovery vs. control mice.**

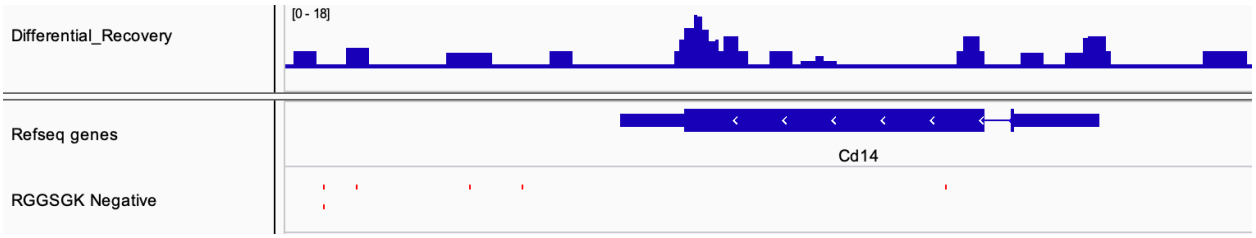

Figure 13: **Motifs for the transcription factor CREM in regions that are differentially accessible at the *Il21* locus in recovered vs. control mice.**

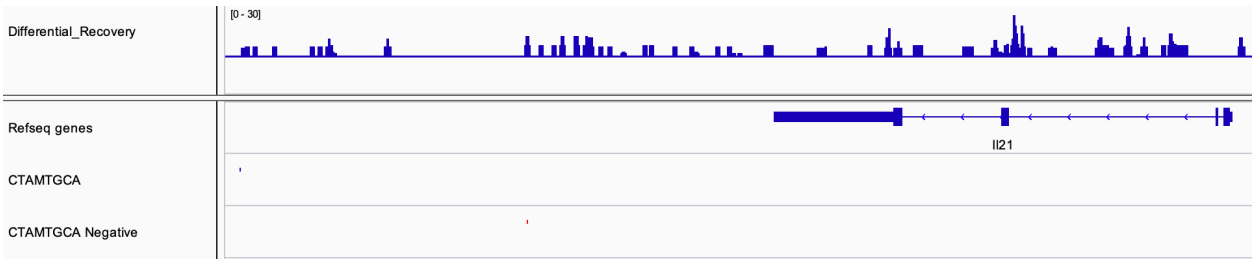

Figure 14: Functional categories enriched in genes with loci differentially accessible in recovered vs. control mice.

	Mus musculus (REF)	upload_1 (Hierarchy) NEW!					
GO biological process complete	#	#	expected	Fold Enrichment	+/-	raw P value	FDR
regulation of microvillus assembly	8	2	.00	> 100	+	1.19E-05	8.62E-03
regulation of microvillus organization	15	2	.01	> 100	+	3.60E-05	1.97E-02
signal transduction involved in regulation of gene expression	23	2	.01	> 100	+	7.93E-05	3.15E-02
positive regulation of transcription by RNA polymerase II	1264	8	.68	11.74	+	4.45E-08	3.54E-04
negative regulation of transcription by RNA polymerase II	866	5	.47	10.71	+	5.69E-05	2.51E-02
positive regulation of transcription, DNA-templated	1581	8	.85	9.39	+	2.51E-07	5.71E-04
regulation of transcription by RNA polymerase II	1977	10	1.07	9.39	+	1.74E-09	2.77E-05
positive regulation of nucleic acid-templated transcription	1585	8	.85	9.36	+	2.56E-07	5.09E-04
positive regulation of RNA biosynthetic process	1586	8	.85	9.36	+	2.58E-07	4.55E-04
negative regulation of transcription, DNA-templated	1204	6	.65	9.25	+	1.77E-05	1.22E-02

Figure 15: Top 10 motifs associated with loci differentially accessible in recovered vs. peak inflammation mice have limited statistical significance.

Rank	Motif	Name	P-value	log P-pvalue	q-value (Benjamini)	# Target Sequences with Motif	% of Targets Sequences with Motif	# Background Sequences with Motif	% of Background Sequences with Motif
1		AS2(LOBAS2)/col-AS2-DAP-Seq(GSE60143)/Homer	1e-4	-1.045e+01	0.0288	103.0	0.16%	165.6	0.11%
2		FOXA1(Forkhead)/LNCAP-FOXA1-ChIP-Seq(GSE27824)/Homer	1e-4	-9.413e+00	0.0406	8486.0	13.49%	20065.4	12.99%
3		FOXM1(Forkhead)/MCF7-FOXM1-ChIP-Seq(GSE72977)/Homer	1e-3	-8.986e+00	0.0415	7112.0	11.31%	16768.9	10.85%
4		ERF13(AP2EREBP)/colamp-ERF13-DAP-Seq(GSE60143)/Homer	1e-3	-8.920e+00	0.0415	2959.0	4.71%	6804.3	4.40%
5		MYB107(MYB)/col-MYB107-DAP-Seq(GSE60143)/Homer	1e-3	-8.094e+00	0.0607	8439.0	13.42%	20022.3	12.96%
6		HOXD13(Homeobox)/Chicken-Hoxd13-ChIP-Seq(GSE38910)/Homer	1e-3	-7.072e+00	0.1406	7567.0	12.03%	17969.3	11.63%
7		OBP1(C2C2dof)/col-OBP1-DAP-Seq(GSE60143)/Homer	1e-3	-7.049e+00	0.1406	20226.0	32.16%	48798.6	31.58%
8		MYB30(MYB)/colamp-MYB30-DAP-Seq(GSE60143)/Homer	1e-2	-6.615e+00	0.1666	5503.0	8.75%	13004.9	8.42%
9		LBD13(LOBAS2)/colamp-LBD13-DAP-Seq(GSE60143)/Homer	1e-2	-6.546e+00	0.1666	2003.0	3.19%	4606.0	2.98%
10		ATY13(MYB)/col-ATY13-DAP-Seq(GSE60143)/Homer	1e-2	-5.995e+00	0.2476	19130.0	30.42%	46210.7	29.91%

Conclusion

This work reveals that, similar to the skin epithelium, chromatin organization in intestinal epithelial cells changes in response to inflammatory damage, and that some of those changes persist for at least 10 days after removal of the inflammatory signal and when the system has healed by physiological (weight) and histological criteria.

There are several directions in which this project could be extended. It remains to be seen whether the epigenetic adaptations actually allow a significantly faster repair response to subsequent rounds of inflammatory damage. First, I hypothesize that adding a second treatment of DSS should result in a faster weight regain during the second recovery period. Second, there is some heterogeneity in the types of ISCs that populate the intestinal crypts, so it would be worthwhile to see whether these different types share the same inflammation-associated open chromatin regions, for example by using single cell ATAC-Seq (Buenrostro et al., 2015) or SHARE-Seq (Ma et al., 2020). Lastly, and more broadly, adaptive epigenetic responses similar to those seen in the skin and the gut might occur in other systems with relatively high regenerative turnover, such as the liver or bone marrow. Identifying other such responses and comparing their underlying mechanisms would be a great contribution to advancing regenerative medicine.

Experimental Methods

Animals

A total of ten WT mice of the Lgr5-EGFP-IRES-creERT2 strain were used in the experiments presented. The initial pilot experiment used two 6-month-old male mice, one as a treatment for calibrating DSS dosing and the other as a negative control. The subsequent time-course experiment used six treatment mice and two control mice. For this experiment, the treatment mice were evenly split male/female and housed in cages by their sex. Two of the male treatment mice were littermates and 5 months old. The third male treatment mouse was 2 months old. All three of the female treatment mice were littermates and 2 months old. The two control mice were also female littermates and 2 months old.

DSS Protocol

Colitis-grade DSS (MP Biomedicals) was dissolved in sterile water at a 3% w/v ratio. This water was then administered to the treatment mice for 7 days. The treatment mice were observed daily for weight loss and increased stool liquidity. After the 7 days of treatment, two mice at peak inflammation were sacrificed. The remaining treatment mice were given normal drinking water during the recovery phase of the experiment. Two mice were sacrificed after 10 days of recovery, and the last two treatment mice were sacrificed after 30 days of recovery. During the recovery period, treatment mice were monitored for weight re-gain and increased solidity in stool composition.

Tissue Processing and Cell Isolation

Mice were euthanized individually with CO_2. Immediately after each euthanization, the small intestine and colon were removed and placed in cold PBS. The insides and outsides of the organs were thoroughly washed in cold PBS. The small intestine and colon were then sliced open, and the internal mucus was manually cleaned off. Samples of the duodenum, ileum, and colon were collected, fixed in formalin, and submitted to the Koch histology facility for H&E staining.

The remainder of the small intestine and colon were dissociated into cell suspensions. The organs were mechanically broken up, and tissue fragments were incubated in 20 mM EDTA-PBS on ice for 90 min, shaking every 30 min. Tissue fragments were then shaken vigorously and incubated in fresh 20 mM EDTA-PBS for 30 min. This step was repeated to finally liberate crypt cells. Tissue fragments were subsequently washed twice in cold PBS to remove EDTA. Crypt cells were centrifuged at 300 rcf for 3 min. Supernatant was removed, and crypt cells were incubated with TrypLE Express Enzyme (ThermoFisher) for 1 min at 37°C. Dissociated crypt cells were then run through a 40 μm filter. Cell count and vitality were assessed using a Countess Automated Cell Counter (Invitrogen). Aliquots of 50,000 crypt cells were collected and stored at -80°C in Bambanker cryopreservation media (Wako Chemicals).

Microscopy

Tissue images were acquired using an Olympus Fluoview FV1200 confocal microscope on bright-field setting. Images were visualized and scale bars overlaid using Metamorph.

ATAC-seq

ATAC-seq was performed on all aliquots by following the Omni-ATAC protocol (Corces et al., 2017). All aliquots consisted of 50,000 cells. The concentrations of ATAC samples were quantified using Qubit and TapeStation. Samples were pooled to create 4 nM ATAC libraries, the final concentrations of which were verified via qPCR. Libraries were denatured and diluted to 1.8 pM prior to sequencing, following Illumina's guidelines. All experimental samples were sequenced with Illumina NextSeq 500/550 v2.5 High Output kits (75 cycles).

Computational Methods

All computational ATAC-seq analyses were performed on the Broad Institute's Terra platform. After each sequencing run, BCL files were demultiplexed and converted to FASTQs. FASTQs were then trimmed of their adapter sequences, aligned to the mm10 reference mouse genome, and processed using the ENCODE ATAC-seq pipeline. To assess sample quality, ATAC signal enrichments around transcription start sites were quantified and fragment size distributions were plotted. Peak calling was performed with MACS2 (Zhang et al., 2008), and where possible, IDR was enabled to refine the peak sets obtained from duplicate biological samples. Motif analysis was conducted on local hardware running HOMER (Heinz et al., 2010), and relevant gene function was determined using the Gene Ontology knowledgebase. Sequencing data tracks and motif locations were visualized with the Broad Institute's IGV application.

References

Barker, N., van de Wetering, M., & Clevers, H. (2008). The intestinal stem cell. *Genes & development*, *22*(14), 1856-1864.

Barker, N., Van Es, J. H., Kuipers, J., Kujala, P., Van Den Born, M., Cozijnsen, M., ... & Clevers, H. (2007). Identification of stem cells in small intestine and colon by marker gene Lgr5. *Nature*, *449*(7165), 1003.

Buchheister, S., Buettner, M., Basic, M., Noack, A., Breves, G., Buchen, B., ... & Bleich, A. (2017). CD14 plays a protective role in experimental inflammatory bowel disease by enhancing intestinal barrier function. *The American journal of pathology*, *187*(5), 1106-1120.

Buenrostro, J. D., Wu, B., Chang, H. Y., & Greenleaf, W. J. (2015). ATAC-seq: a method for assaying chromatin accessibility genome-wide. *Current protocols in molecular biology*, *109*(1), 21-29.

Buenrostro, J. D., Wu, B., Litzenburger, U. M., Ruff, D., Gonzales, M. L., Snyder, M. P., ... & Greenleaf, W. J. (2015). Single-cell chromatin accessibility reveals principles of regulatory variation. *Nature*, *523*(7561), 486-490.

Chassaing, B., Aitken, J. D., Malleshappa, M., & Vijay-Kumar, M. (2014). Dextran sulfate sodium (DSS)-induced colitis in mice. *Current protocols in immunology*, *104*(1), 15-25.

Chen, L., Vasoya, R. P., Toke, N. H., Parthasarathy, A., Luo, S., Chiles, E., ... & Verzi, M. P. (2020). HNF4 regulates fatty acid oxidation and is required for renewal of intestinal stem cells in mice. *Gastroenterology*, *158*(4), 985-999.

Cheng, H., & Leblond, C. P. (1974). Origin, differentiation and renewal of the four main epithelial cell types in the mouse small intestine V. Unitarian theory of the origin of the four epithelial cell types. *American Journal of Anatomy*, *141*(4), 537-561.

Clevers, H. (2013). The intestinal crypt, a prototype stem cell compartment. *Cell*, *154*(2), 274-284.

Corces, M. R., Trevino, A. E., Hamilton, E. G., Greenside, P. G., Sinnott-Armstrong, N. A., Vesuna, S., ... & Kathiria, A. (2017). Omni-ATAC-seq: improved ATAC-seq protocol.

Heinz, S., Benner, C., Spann, N., Bertolino, E., Lin, Y. C., Laslo, P., ... & Glass, C. K. (2010). Simple combinations of lineage-determining transcription factors prime cis-regulatory elements required for macrophage and B cell identities. *Molecular cell*, *38*(4), 576-589.

Jadhav, U., Saxena, M., O'Neill, N. K., Saadatpour, A., Yuan, G. C., Herbert, Z., ... & Shivdasani, R. A. (2017). Dynamic reorganization of chromatin accessibility signatures during dedifferentiation of secretory precursors into Lgr5+ intestinal stem cells. *Cell Stem Cell*, *21*(1), 65-77.

Jedlicka, P., & Gutierrez-Hartmann, A. (2008). Ets transcription factors in intestinal morphogenesis, homeostasis and disease. *Histology and histopathology*, *23*(11), 1417.

Kaur, P., & Potten, C. S. (1986). Effects of puromycin, cycloheximide and noradrenaline on cell migration within the crypts and on the villi of the small intestine. *Cell Proliferation*, *19*(6), 611-625.

Kim, T. H., Li, F., Ferreiro-Neira, I., Ho, L. L., Luyten, A., Nalapareddy, K., ... & Shivdasani, R. A. (2014). Broadly permissive intestinal chromatin underlies lateral inhibition and cell plasticity. *Nature*, *506*(7489), 511.

Kim, C. K., Saxena, M., Maharjan, K., Song, J. J., Shroyer, K. R., Bialkowska, A. B., ... & Yang, V. W. (2020). Krüppel-like factor 5 regulates stemness, lineage specification, and regeneration of intestinal epithelial stem cells. *Cellular and molecular gastroenterology and hepatology*, *9*(4), 587-609.

Ma, S., Zhang, B., LaFave, L. M., Earl, A. S., Chiang, Z., Hu, Y., ... & Buenrostro, J. D. (2020). Chromatin Potential Identified by Shared Single-Cell Profiling of RNA and Chromatin. *Cell*, *183*(4), 1103-1116.

Naik, S., Larsen, S. B., Cowley, C. J., & Fuchs, E. (2018). Two to Tango: Dialog between Immunity and Stem Cells in Health and Disease. *Cell*, *175*(4), 908-920.

Naik, S., Larsen, S. B., Gomez, N. C., Alaverdyan, K., Sendoel, A., Yuan, S., ... & Fuchs, E. (2017). Inflammatory memory sensitizes skin epithelial stem cells to tissue damage. *Nature*, *550*(7677), 475.

Ohl, K., Wiener, A., Lippe, R., Schippers, A., Zorn, C., Roth, J., ... & Tenbrock, K. (2016). CREM alpha enhances IL-21 production in T cells in vivo and in vitro. *Frontiers in immunology*, *7*, 618.

Richmond, C. A., Rickner, H., Shah, M. S., Ediger, T., Deary, L., Zhou, F., ... & Breault, D. T. (2018). JAK/STAT-1 signaling is required for reserve intestinal stem cell activation during intestinal regeneration following acute inflammation. *Stem cell reports*, *10*(1), 17-26.

Santos, A. J., Lo, Y. H., Mah, A. T., & Kuo, C. J. (2018). The Intestinal Stem Cell Niche: Homeostasis and Adaptations. *Trends in cell biology*.

Shi, Y. J., Gong, H. F., Zhao, Q. Q., Liu, X. S., Liu, C., & Wang, H. (2019). Critical role of toll-like receptor 4 (TLR4) in dextran sulfate sodium (DSS)-induced intestinal injury and repair. *Toxicology letters*, *315*, 23-30.

Tetteh, P. W., Basak, O., Farin, H. F., Wiebrands, K., Kretzschmar, K., Begthel, H., ... & Van Oudenaarden, A. (2016). Replacement of lost Lgr5-positive stem cells through plasticity of their enterocyte-lineage daughters. *Cell stem cell*, *18*(2), 203-213.

Tian, H., Biehs, B., Warming, S., Leong, K. G., Rangell, L., Klein, O. D., & de Sauvage, F. J. (2011). A reserve stem cell population in small intestine renders Lgr5-positive cells dispensable. *Nature*, *478*(7368), 255.

Williams, J. M., Duckworth, C. A., Burkitt, M. D., Watson, A. J. M., Campbell, B. J., & Pritchard, D. M. (2015). Epithelial cell shedding and barrier function: a matter of life and death at the small intestinal villus tip. *Veterinary pathology*, *52*(3), 445-455.

Xie, J., Li, L., Deng, S., Chen, J., Gu, Q., Su, H., ... & Zhang, Q. (2020). Slit2/Robo1 Mitigates DSS-induced Ulcerative Colitis by Activating Autophagy in Intestinal Stem Cell. *International journal of biological sciences*, *16*(11), 1876.

Zhang, Y., Liu, T., Meyer, C. A., Eeckhoute, J., Johnson, D. S., Bernstein, B. E., ... & Liu, X. S. (2008). Model-based analysis of ChIP-Seq (MACS). *Genome biology*, *9*(9), 1-9.

Zschemisch, N. H., Brüsch, I., Hambusch, A. S., & Bleich, A. (2016). Transcription factor SP2 enhanced the expression of Cd14 in colitis-susceptible C3H/HeJBir. *PloS one*, *11*(5), e0155821.